Estuarine residual flow induced by eddy viscosity-shear covariance: Dependence on axial bottom slope, tidal intensity and constituents

W. Chen[a,b,*], H.E. de Swart[a]

[a] Institute for Marine and Atmospheric Research, Utrecht University, Princetonplein 5, 3584 CC Utrecht, the Netherlands
[b] Helmholtz Institute, Max-Planck-Straße 1, 21502 Geesthacht, Germany

A B S T R A C T

Residual flow generated by Eddy viscosity-Shear Covariance (ESCO) in a narrow estuary is investigated with a numerical model. New aspects concern the dependence of the spatial structure of ESCO flow on (1) longitudinal depth variation for fixed semi-diurnal tidal forcing, (2) varying amplitude of the semi-diurnal tidal forcing, and (3) mixed tidal forcing for fixed stratification at the mouth. Regarding (1) and (2), it appears that ESCO flow merely involves the components due to the semi-diurnal tide (u_{τ,M_2}) and quarter-diurnal tide (u_{τ,M_4}). For a periodically stratified estuary, u_{τ,M_2} is stronger than u_{τ,M_4} in the middle reach, and weaker in the other reaches, while both show a two-layer structure with seaward flow near the surface. For weak stratification, u_{τ,M_2} has a three-layer structure with seaward flow in the middle layer, while u_{τ,M_4} has a two-layer structure and contributes significantly to the total residual flow in the upper and lower reach. For a highly stratified estuary, u_{τ,M_2} dominates the ESCO flow (being weak compared to the total residual flow), and it has a reversed two-layer structure (seaward flow near the bottom). Regarding (3), if diurnal and semi-diurnal tides are of similar order, the ESCO flow due to diurnal tides dominates and it has a two-layer structure. If diurnal tides prevail, the ESCO flow induced by the long-periodic tide (due to joint action of two diurnal tides) is the main contributor to the total residual flow in the upper and lower reach of the estuary.

1. Introduction

It has been noted in many studies that residual flow, driven by a shear stress that is due to the covariance between tidally varying eddy viscosity and the vertical gradient of tidal velocity, is a significant component of the estuarine circulation (Jay and Musiak, 1994; Stacey et al., 2001, 2008, 2010; Burchard and Hetland, 2010; Burchard and Schuttelaars, 2012; Cheng et al., 2010; Geyer and MacCready, 2014). Following Dijkstra et al. (2017), this covariance is referred to as 'Eddy viscosity Shear COvariance' (ESCO). Clearly, eddy viscosity varies during the tidal cycle, e.g. it peaks at both maximum flood and maximum ebb. Besides, another type of temporal variation of eddy viscosity results from the advection of the density field by horizontal currents that have vertical shear (de Ruijter, 1983; van Aken, 1986; Simpson et al., 1990). In the case of tidal currents, during flood, salt oceanic water is strained over fresher water, causing stratification to decrease, thereby resulting in increased turbulence. In contrast, during ebb, relatively light water is advected over salt water, the stratification is enhanced and this suppresses turbulence. In tidally energetic estuaries, this so-called tidal straining mechanism results in variation of eddy

viscosity at the period of the primary tide, which is often the semi-diurnal M_2 tide (Burchard and Baumert, 1998; Geyer et al., 2000; Stacey et al., 2001; Simpson et al., 2002, 2005; Pein et al., 2014).

The background stratification of the water column has a strong impact on the temporal variation of turbulent eddy viscosity that results from the straining process, and thereby on the structure of the residual flow that is driven by ESCO. Using a 1D numerical model, Stacey et al. (2008) found that in a periodically stratified water column, the ESCO flow always shows a two-layer structure in the vertical direction, with the flow direction in the layers depending on the tidal phase at which a perturbation in the density field is externally imposed. The onset of stratification during the ebb phase results in landward flow near the bottom and seaward flow near the surface. This is referred to as a 'classical' two-layer structure, because it is identical to that of the estuarine circulation driven by horizontal density gradients. However, if stratification is imposed during the flood phase, the ESCO flow has a 'reversed' two-layer structure (landward directed in the upper layer and seaward below it). Similar findings were reported by Cheng et al. (2010), who investigated the ESCO flow in weakly stratified to highly stratified estuaries by using a 3D numerical model (Cheng et al., 2011,

2013), in which the variation in stratification was computed internally, rather than being imposed. The degree of stratification in the estuary is controlled by a varying amplitude of a single externally forced tide, i.e., the semi-diurnal tide. Their results show that under periodically stratified conditions the residual flow due to ESCO has a classical two-layer structure. If stratification increases, first a transition to a three-layer structure occurs, and for highly stratified conditions a reversed two-layer structure is obtained. Note that the tidal mean stratification not only affects the temporal evolution of turbulent eddy viscosity, but also the vertical shear of the semi-diurnal tidal current (Chen and de Swart, 2016), which is also a part of ESCO.

Apart from tidal straining, the covariance between eddy viscosity and tidal velocity shear could also result from, e.g., tidal variation of eddy viscosity induced by wind (Verspecht et al., 2009). Recently, Dijkstra et al. (2017) showed with 1D and 2D numerical models that at a specific location in the (partially stratified and M_2 dominated) Scheldt River Estuary, the covariance between M_4 eddy viscosity and M_4 tidal velocity shear contributes about 8% to the total residual flow (other drivers of residual flow are horizontal density gradients, Stokes transport, etc.). Sources of M_4 tidal velocity are, e.g., nonlinear advection of the M_2 tidal momentum by M_2 tidal currents and depth dependent friction (e.g. Ianniello, 1977). The M_4 eddy viscosity component is generated by the friction velocity of the M_2 tide, and by intratidal variations of the density stratification (Simpson et al., 2005).

So far, the studies on ESCO mainly considered estuaries of constant depth with the M_2 being the dominant tide and the ESCO flow was analysed at fixed locations. These observations motivate three research aims of the present study. First (RA.1), to investigate the effect of longitudinal depth variation on the structure of ESCO flow for fixed tidal forcing that consists of a single semi-diurnal constituent. Second (RA.2), to quantify the effect of tidal mean stratification on the ESCO flow at all locations in the estuary. Third (RA.3), to investigate the ESCO-induced residual flow in the case that the externally forced tide contains multiple constituents with frequencies that do not have an integer ratio and stratification at the mouth is kept fixed. The latter is relevant because tidal forces generate not only M_2, but also e.g. diurnal constituents P_1, K_1 and O_1 and a semi-diurnal constituent S_2. As highlighted by Geyer and MacCready (2014), systematic investigation of dynamics of estuaries in which the tidal motion is forced by multiple constituents is "surprisingly" late. One consequence of including diurnal tide is that the straining of isohaline in tidal cycles causes a diurnal component in eddy viscosity. Another important consequence of the joint action of tidal constituents with different frequencies is that nonlinear interactions between any two single tidal constituents will influence other tidal constituents and generate new constituents, in particular a long-periodic tide, which also contribute to the ESCO residual flow.

To address these objectives, the numerical model Delft3D-FLOW (Lesser et al., 2004) is applied to explicitly resolve the temporal and spatial structure of vertical eddy viscosity and tidal flow at different locations. The focus of this work is on the longitudinal dynamics driven by tides. Hence, the estuary is assumed to be straight and narrow, without lateral variations in depth. Moreover, effects of wind and the Coriolis force are not considered. The latter conditions imply a weak lateral flow, which also causes straining of the density field (e.g. Lacy et al., 2003; Burchard and Schuttelaars, 2012; Basdurak et al., 2013).

In Section 2, the numerical model and the design of the experiments are presented. Furthermore, the methods to calculate residual flow induced by ESCO, and to decompose the ESCO forcing into contributions due to different tidal constituents are described. Model results are presented in Section 3, followed by a discussion in Section 4. Finally, Section 5 contains the conclusions.
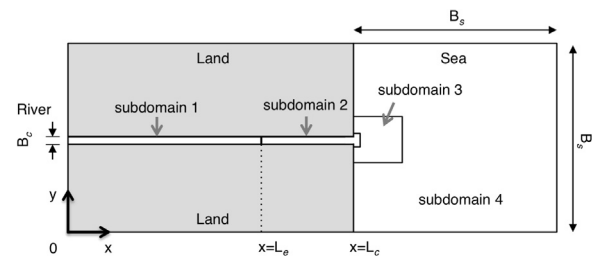

Fig. 1. Geometry of the idealised estuary-shelf sea system. The subdomains are introduced for reasons of numerical efficiency (see text for details).

2. Material and methods

2.1. Model

The numerical hydrodynamic model Delft3D-FLOW (for a description, see (Delft, 2006)) is used to simulate currents, salinity and turbulence in an idealised estuary-shelf system (Fig. 1). Temperature is kept constant so that density variations are due to salinity variations only. An x, y, σ-coordinate system is adopted, in which $\sigma = (z - \eta)/D$, with $z = \eta$ being the vertical level of the free-surface, D being the distance from free-surface to the bottom and x, y, z are Cartesian coordinates. The straight channel is located between river head $x = 0$ and estuary mouth $x = L_c$. It has an undisturbed depth $H(x)$ and a constant width B_c. The adjacent sea has straight open boundaries that are positioned at a distance B_s from the estuary mouth and it has a depth that increases linearly from the coast to the eastern boundary. Freshwater is prescribed at the estuary head $x = 0$ with a constant discharge Q. At the three open boundaries of the sea, tidal sea surface elevations with given amplitudes and frequencies are imposed. Moreover, fixed values of salinity are imposed at these boundaries. A two-equation $k - \varepsilon$ turbulence scheme is used to compute vertical eddy viscosity and eddy diffusivity. Horizontal eddy viscosity and diffusivity are assumed to be constant.

2.2. Setup of experiments

First, a setting of experiments is designed to address the first research aim (RA.1). For this, a fixed river discharge is prescribed at the landward side, while at the seaward boundaries a tide is imposed with a single frequency that in each boundary point has the same amplitude and phase. Furthermore, the bottom is flat from river head to the location $x = L_e$, which is inside the estuary (see Fig. 1), whilst seaward of this location water depth linearly increases to the estuary mouth ($x = L_c$) with different values of the bottom slope. Three different series of experiments are considered. In the first series, the depth $H_e = H(x = L_e)$ is kept fixed and $H_c = H(x = L_c)$ increases with increasing bottom slope. In series 2, The depth in the middle of the estuary ($x = (L_e + L_c)/2$) is fixed, H_e decreases and H_c increases such that the volume of the estuary is kept fixed. Finally, in series 3, H_e decreases and H_c is kept fixed.

The fourth series of experiments is designed to address the second research aim (RA.2). To focus on the effect of varying tidal mean stratification on the spatial structure of the ESCO flow, a constant depth is used between river head and estuary mouth. The forcing is identical to that of the previous series, but now the amplitude of the tide at the open boundaries is varied, such that a different degree of stratification is obtained in the estuary.

Finally, the fifth series of experiments addresses the third research aim (RA.3), i.e., to assess the spatial structure of the ESCO flow in an estuary in which tidal motion is driven by tides imposed at the seaward boundaries that contain multiple constituents with different amplitudes. The constituents that are considered are a semi-diurnal tide with radian frequency ω and two diurnal tidal constituents with frequencies

Table 1

The framework of the model experiments design.

Aim	Experiments	Controlled conditions							
		Bottom slope	Tidal constituents	Tidal amplitude (m)					
RA.1	Series 1, 2, 3	Range from 0 to 1×10^{-4} at intervals of 2.5×10^{-5}.	semi-diurnal	Fixed at the open boundaries.					
RA.2	Series 4	Fixed (no slope)	semi-diurnal	Range from 0.5 m to 1.5 m at intervals of 0.05 m.					
RA.3	Series 5	Fixed (no slope)	semi-diurnal	0.75	0.73	0.70	0.65	0.60	0.55	0.35	0.00
			diurnal	0.00	0.10	0.20	0.35	0.50	0.65	0.80	0.90

$\frac{1}{2}\omega - \Delta\omega$ and $\frac{1}{2}\omega + \Delta\omega$, respectively, where $\Delta\omega$ is a constant. The reason for this choice is that including two diurnal tidal constituents will create spring-neap cycles in tidal currents with period $\pi/\Delta\omega$. Selecting only one semi-diurnal tide will avoid additional spring-neap cycles, which would complicate the analysis. In this series, different values of amplitudes of semi-diurnal tide and diurnal tides at the open boundaries are chosen, such that the amplitude ratio between diurnal tides and semi-diurnal tides changes from 0 to 1, while the amplitude of the friction velocity at the mouth of the estuary, U_*, is fixed (see Section 2.6 for details). The latter is done because U_* is used to indicate the intensity of external tidal forcing of the estuary.

The relations between the research aims and the series of experiments are summarised in Table 1. The model input parameters that are constant for all experiments are listed in Table 2. These values are representative for a typical single channel tidal estuary. In the experiments of series 1, 2 and 3, the tidal amplitude is 1 m at the three open boundaries. In series 1, depth is fixed at 10 m at the river side entrance ($x = L_e$), and it increases towards the mouth ($x = L_c$). In series 2, depth is fixed at 10 m at the middle estuary ($x = (L_e + L_c)/2$), it decreases towards $x = L_e$ but increases towards $x = L_c$. In series 3, fixed depth is fixed at 10 m at $x = L_c$ and decreases towards $x = L_e$. Recall that the depth for $x < L_e$ equals that at $x = L_e$. In the experiments of series 4 and 5, a constant depth $H = 10$ m is applied for the entire channel ($0 < x < L_c$).

For reasons of numerical efficiency, the semi-diurnal tide (hereafter called $M_{2'}$) is assumed to have a radian frequency $\omega = 1.45 \times 10^{-4}$ s^{-1} (i.e., with a period of 12 h). Likewise, the two diurnal tidal constituents are called $O_{1'}$ and $K_{1'}$, respectively. Furthermore, for series 5, a strict tidal mean (to compute tidal residual flow) can only be calculated if $\omega/\Delta\omega$ is an integer ratio. The larger this ratio, the longer the period over which the tidal mean has to be computed. To avoid long computational times of the tidal mean, $\Delta\omega$ is adjusted in such a way that both diurnal and semi-diurnal constituents repeat themselves after a single spring-neap cycle (with period $\pi/\Delta\omega$). As is shown in Table 2, $\Delta\omega = \omega/18$ yields a spring-neap tidal cycle of 4.5 days. The values of tidal amplitudes ($A_{M_{2'}}$, etc.) of all tidal constituents ($M_{2'}$, …) are given in Table 1.

The model is spun up from rest, with $S = 31$ psu everywhere in the domain and runs span a time that is sufficiently long to ensure that the

transient effects of initial conditions are no longer present. This was verified in series 1–4 by comparing the results from the last tidal cycle with those of the previous one. In series 5, this was done by comparing the results of the last spring-neap cycle with those of the preceding cycle.

2.3. Numerical aspects

To increase the efficiency of the model computation, the model domain is divided into four subdomains (Fig. 1). All subdomains have 20 sigma layers that are uniformly divided in the vertical direction. The grid cells in all subdomains have the same size in $x-$ and $y-$ direction. The ratio between the horizontal grid sizes of two adjacent subdomains (the value of the larger grid size over the smaller grid size) is 3. The first subdomain is from $x = 0$ to $x = L_e$. Here, the number of grid points in each $\sigma-$ layer is 282 (along-channel) by 6 (across-channel) and the longitudinal grid size is 750 m. Subdomain 2 is from $x = L_e$ to $x = L_c + l$, where $l = 3$ km. It has in each σ-layer of 200 by 12 grid points in the channel and 14 by 26 grid points on the shelf. The longitudinal grid size is 250 m. For each σ-layer, in the two horizontal directions, subdomain 3 consists of 38 grid points and subdomain 4 contains 46 grid points. The longitudinal grid sizes in subdomains 3 and 4 are 750 m and 2.25 km, respectively. Here, the relatively smaller grid size around the corner of the estuary mouth allows detailed simulation of the hydrodynamics around the estuarine mouth.

2.4. Decomposition of residual flow

The residual flow contains components that are generated by different drivers, e.g., river discharge, horizontal density gradients and nonlinear advection of tidal momentum by tidal flow (Geyer and MacCready, 2014). To identify the residual flow induced by ESCO, the tidally mean longitudinal momentum equation and continuity equation are considered that only include the ESCO forcing (Burchard and Hetland, 2010; Cheng et al., 2013). The solutions of these equations read

$$u_\tau = \int_{-1}^{\sigma} H \frac{1}{\overline{A_v}} \left(gH \frac{\partial \eta_\tau}{\partial x} \tilde{\sigma} - \tau \right) d\tilde{\sigma}, \tag{1a}$$

$$\frac{\partial \eta_\tau}{\partial x} = \int_{-1}^{0} \int_{-1}^{\sigma} H \frac{\tau}{\overline{A_v}} d\tilde{\sigma} d\sigma / \int_{-1}^{0} \int_{-1}^{\sigma} gH^2 \frac{\tilde{\sigma}}{\overline{A_v}} d\tilde{\sigma} d\sigma, \tag{1b}$$

in which

$$\tau = \frac{1}{H} \overline{A'_v \frac{\partial u'}{\partial \sigma}} + \tau_a, \tag{2a}$$

$$\tau_a = \int_{\sigma}^{0} \left[\frac{2\eta}{H^2} \frac{\partial}{\partial \tilde{\sigma}} \left(\overline{A_v \frac{\partial u'}{\partial \tilde{\sigma}}} \right) + \frac{2\eta}{H^2} \frac{\partial}{\partial \tilde{\sigma}} \left(A'_v \frac{\partial \overline{u}}{\partial \tilde{\sigma}} \right) + \frac{2\eta}{H^2} \frac{\partial}{\partial \tilde{\sigma}} \left(A'_v \frac{\partial u'}{\partial \tilde{\sigma}} \right) \right] d\tilde{\sigma}. \tag{2b}$$

Here, $\tilde{\sigma}$ is a dummy variable, and the overbar $\overline{(\cdot)}$ and prime $(')$ represent the tidally averaged and tidally varying part of a variable, respectively. The sea surface gradient $\frac{\partial \eta_\tau}{\partial x}$ is such that there is no mass transport by u_τ through the cross-section, as follows from mass conservation. The vertical eddy viscosity is denoted by A_v and g (=9.8 ms^{-2}) is the

Table 2

Values of the model input parameters.

Parameter	Symbol	Unit	Value
Channel length	L_c	km	260
Channel width	B_c	km	3
River section length	L_e	km	210
Depth at eastern seaward boundary	H_{sea}	m	50
Shelf sea size	B_s	km	100
Freshwater discharge	Q	m^3 s^{-1}	1500
Salinity at open boundaries	S	psu	31
Background temperature	T	°C	15
Horizontal eddy viscosity	A_h	m^2 s^{-1}	50
Horizontal eddy diffusivity	K_h	m^2 s^{-1}	50
Semi-diurnal tidal frequency	ω	s^{-1}	1.45×10^{-4}
Half of spring-neap tidal frequency	$\Delta\omega$	s^{-1}	8.06×10^{-6}

gravitational acceleration. The first component inside brackets in the r.h.s. of Eq. (1a) contains the barotropic pressure gradient. Variable τ is a (kinematic) mean stress that is defined in Eq. (2a). The first part on the r.h.s of Eq. (2a) represents the covariance between time-varying eddy viscosity and vertical tidal velocity shear at fixed σ-levels (ESCO$^\sigma$). The second term τ_a is given in Eq. (2b). It is related to the covariance between the time-varying water surface elevation η and tidal shear, water surface elevation and eddy viscosity and triple covariance between water surface elevation, eddy viscosity, and vertical shear, respectively. The contribution τ_a to τ results from using σ-coordinates rather than $z-$ coordinates.

2.5. Quantification of stratification in the estuary

The degree of stratification in the estuary is determined by the competition between buoyancy forcing and tidal forcing. In this study, the former is due to freshwater input and the latter is quantified by the friction velocity at the mouth of the estuary. Following Geyer and MacCready (2014), in the cases that the tidal forcing has a dominant constituent, two parameters Fr_f and M are used that control the degree of stratification at the mouth, i.e.,

$$Fr_f = \frac{U_R}{N_0 H_c}, \quad \text{and} \quad M = \frac{U_*}{(\omega N_0)^{1/2} H_c}. \tag{3}$$

Here, Fr_f is the freshwater Froude number, which expresses a ratio between the river flow U_R ($= \frac{Q}{H_c B_c}$) and the scale of the maximum possible frontal propagation speed. In Eq. (3), $N_0 = (\beta g S/H_c)^{1/2}$, with H_c the depth at the mouth, is an estimate of the buoyancy frequency in the case of maximum top-to-bottom salinity variation in an estuary, in which S is the salinity at the open boundaries and $\beta = 7.8 \times 10^{-4} \text{psu}^{-1}$ is the salinity contraction coefficient. The second parameter M expresses the ratio of the tidal timescale to the vertical turbulent mixing timescale at the mouth.

In this study, the parameters Fr_f and M are used to classify the estuary, based on the regime diagram shown in Geyer and MacCready (2014). However, Fr_f and M do not yield information about the degree of stratification at the locations inside the estuary. For this reason, an alternative parameter, $\Delta S/S$ is used, in which ΔS is the tidal mean top-to-bottom salinity difference that depends on x, and $S = 31$ psu is the salinity at the open boundaries.

2.6. Mixed tidal forcing

In case that the tidal forcing contains $M_{2'}$, $O_{1'}$ and $K_{1'}$, nonlinear interactions between these constituents will result in additional constituents with sum and difference frequencies. For example, quadratic nonlinear terms (like advection) generate additional constituents like ter-diurnal tides ($MO_{3'}$ and $MK_{3'}$), a quarter-diurnal tide ($M_{4'}$) and a long-periodic tide (Mf'). Note that nonlinear interaction involving these new constituents will further result in additional constituents, e.g. the interaction of $M_{2'}$ and $M_{4'}$ will generate an $M_{6'}$ tide.

The characteristics of the forced mixed tide are measured by parameter

$$F' = \frac{F}{1+F} \quad \text{and} \quad F = \frac{\sqrt{U_{m,O_{1'}}^2 + U_{m,K_{1'}}^2}}{\sqrt{U_{m,M_{2'}}^2 + U_{m,O_{2'}}^2 + U_{m,K_{2'}}^2}}. \tag{4}$$

Here, F was introduced by Defant (1958) and it measures the ratio of the maximum diurnal tidal amplitude and that of the semi-diurnal tide. In Eq. (4), $U_m = U_*/C_d^{1/2}$ (where $C_d \simeq 1 - 2.5 \times 10^{-3}$ denotes a drag coefficient) is the cross-sectional mean tidal current amplitude at the estuary mouth. When $0.2 < F' < 0.75$, the tidal motion is considered as a mixed tide. The tide is considered semi-diurnal dominant when $0 < F' < 0.2$, and diurnal dominant when $0.75 < F' < 1$.

2.7. Harmonic analysis

Harmonic analysis is used in order to quantify the relative contribution of different tidal constituents to the total signal. Below, the kinematic shear stress component ESCO$^\sigma$ is considered (the first term of Eq. (2a)). Consequently, the harmonic decomposition is applied to the time series of the velocity shear ($\frac{1}{H}\frac{\partial u'}{\partial \sigma}$) and the vertical eddy viscosity (A'_v), respectively. This yields

$$\frac{1}{H}\frac{\partial u'}{\partial \sigma} = \sum_n \frac{1}{H}\left[\frac{\partial u_n}{\partial \sigma}\right]\cos\left(\omega_n t - \varphi_n\right), \tag{5a}$$

$$A_{v'} = \sum_n A_{v,n}\cos\left(\omega_n t - \psi_n\right), \tag{5b}$$

where $\frac{1}{H}\left[\frac{\partial u_n}{\partial \sigma}\right]$ denotes the amplitude of the vertical shear of tidal velocity of a specific tidal constituent ($O_{1'}$, $K_{1'}$, $M_{2'}$, $M_{4'}$, ...). Furthermore, ω_n is the radian frequency and φ_n is the phase. Similarly, $A_{v,n}$ and ψ_n are the amplitude and phase of eddy viscosity of the tidal harmonic n, respectively.

Substitution of Eq. (5) and 5b into Eq. (2a) (and ignoring ESCO^a at this stage) yields

$$\tau = \underbrace{\tau_{O_{1'}} + \tau_{K_{1'}}}_{diurnal} + \underbrace{\tau_{O_{2'}} + \tau_{K_{2'}} + \tau_{M_{2'}}}_{semi-diurnal} + \underbrace{\tau_{MO_{3'}} + \tau_{MK_{3'}}}_{ter-diurnal} + \underbrace{\tau_{M_{4'}}}_{quarter-diurnal} + ..., \tag{6}$$

with

$$\tau_n = \frac{1}{H}A_{v,n}\left[\frac{\partial u_n}{\partial \sigma}\right]\frac{1}{2}\cos\left(\varphi_n - \psi_n\right). \tag{7}$$

Similarly, the term τ_a in Eq. (2a) is decomposed into contributions due to different tidal constituents. The ESCO flow components and corresponding sea surface gradients are

$$u_{\tau,n} = \int_{-1}^{\sigma} H\frac{1}{\overline{A}_v}\left(gH\frac{\partial\eta_{\tau,n}}{\partial x}\tilde{\sigma} - \tau_n\right)d\tilde{\sigma}, \tag{8a}$$

$$\frac{\partial\eta_{\tau,n}}{\partial x} = \int_{-1}^{0}\int_{-1}^{\sigma}H\frac{\tau_n}{\overline{A}_v}d\tilde{\sigma}d\sigma \Big/ \int_{-1}^{0}\int_{-1}^{\sigma}gH^2\frac{\tilde{\sigma}}{\overline{A}_v}d\tilde{\sigma}d\sigma. \tag{8b}$$

In Eq. (8a), $u_{\tau,n}$ denote the residual flows generated by ESCO due to individual tidal frequencies, with n representing $O_{1'}$, $K_{1'}$, $M_{2'}$, $M_{4'}$, ... The sea surface gradients $\frac{\partial\eta_{\tau,n}}{\partial x}$ in Eq. (8b) is related to $u_{\tau,n}$.

2.8. Quantifying the importance of the ESCO flow due to individual tides and their structures

The relative importance of the residual flow induced by ESCO of individual harmonic frequencies with respect to the total ESCO flow is computed as

$$r_n = \frac{\frac{1}{2}\int_{-1}^{0}u_{\tau,n}^2 d\sigma}{\sum\frac{1}{2}\int_{-1}^{0}u_{\tau,m}^2 d\sigma}. \tag{9}$$

Parameter r_n measures the ratio between the depth-integrated kinetic energies of one ESCO flow component and the sum of the depth-integrated kinetic energy of all ESCO flow components. The ESCO flow due to an individual tide is considered as a dominant component when $r_n > 0.5$. Furthermore, the ESCO flow due to an individual tide is small when $r_n < 0.05$.

Likewise, the relative importance of the ESCO flow with respect to the residual flow due to other drivers (e.g., river flow, density driven flow etc.) is computed as

$$r_E = \frac{\frac{1}{2}\int_{-1}^{0}u_\tau^2 d\sigma}{\frac{1}{2}\int_{-1}^{0}\overline{u}^2 d\sigma}, \tag{10}$$
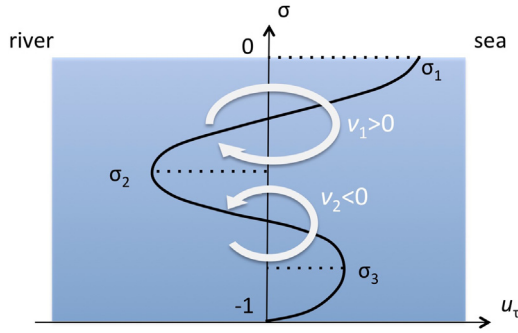
Fig. 2. Example of an ESCO flow that is characterised by three flow layers and two vorticity layers. Positive (negative) values of the ESCO flow (black line) is seaward (landward). Overturning of the flow is indicated by white arrows.

where $\bar{u}$ is the total residual flow. The ESCO flow is considered relevant when $r_E > 0.05$.

To indicate the structure of ESCO flows, first, layers are identified in which the vorticity $\frac{1}{H}\frac{\partial u_\tau}{\partial \sigma}$ has a fixed sign. This is done because vorticity is a measure of the degree of overturning in such a layer. For the classical estuarine circulation there is one layer in which the vorticity is positive if seaward flow is defined as positive. The boundaries of these layers $\sigma_i (i = 1, 2, \dots I - 1$, ordered from surface to bottom) are defined as the levels at which u_τ attains an extremum $u_{\tau,i}$. Here, $I \geq 2$ denotes the total number of extreme values in the vertical profiles of u_τ. Next, a measure of the vorticity $\mathscr{V}_i$ is calculated as

$$\mathscr{V}_i = \frac{u_{\tau,i} - u_{\tau,i+1}}{H(\sigma_i - \sigma_{i+1})}. \tag{11}$$

Note that at the bottom ($\sigma = -1$), $u_\tau = 0$ is not accounted for in the calculation of the vorticity. Positive (negative) $\mathscr{V}_i$ denotes clockwise (anti-clockwise) overturning (Fig. 2). The velocity has an extremum at the surface ($\sigma = \sigma_1 = 0$), thus the upper vorticity layer extends from the surface downward to the location $\sigma = \sigma_2$, where the next extremum in the velocity occurs. When there are three velocity layers, the lower vorticity layer exists from the first extremum (σ_2) to the third extremum (σ_3) in velocity profile.

3. Results

3.1. Structure of u_τ for varying longitudinal depth (RA.1)

Fig. 3 shows results for model runs with a flat bottom (first experiment of series 1 in Table 1) and a bottom with a slope of 1×10^{-4} (last experiment of series 1 in Table 1). The computed Fr_f and M are 3.2×10^{-2} and 1.2 for the former case, respectively, 1.8×10^{-2} and 0.64 for the latter case. Upon tracing these values in the regime diagram of Geyer and MacCready (2014), it follows that the estuary is periodically stratified in the flat bottom case and it is at the transition between weakly stratified to highly stratified in the sloping bottom case. In panels (a) and (b), the degree of stratification $\Delta S/S$ and the strength of the ESCO flow with respect to total residual flow r_E are plotted as a function of longitudinal distance. In both cases, $\Delta S/S$ increases from zero at the riverside up to the maximum value at 254 km, and subsequently decreases to the estuary mouth. At each location, the value of $\Delta S/S$ in the latter case is larger than that in the former case. Two distinct structures are identified in u_τ for the two model configurations. Note that results are shown in the part of the estuary where the value of $\Delta S/S$ varies in the longitudinal direction. In the flat bottom case (Fig. 3c), a two-layer structure is observed with landward flow near the bottom and seaward flow near the surface. In the case of the sloping bottom (Fig. 3d), a three-layer structure is found, with landward flow both near the surface and near the bottom, and seaward flow in the middle. Panels (e) and (f) show the longitudinal distribution of the total residual flow for the two cases. Comparing (c) with (e) and (d) with (f) reveals that the contribution of the ESCO flow to the total residual flow is relevant ($r_E > 0.05$) between 252 km and 260 km in the flat bottom case and between 239 km and 259 km in the sloping bottom case (Fig. 3a and b).

Harmonic analysis of ESCO$^\sigma$ identifies two main contributions to u_τ, i.e., the ESCO flow due to the M$_{2'}$ tide ($u_{\tau,M_{2'}}$) and that due to the M$_{4'}$ tide ($u_{\tau,M_{4'}}$). The relative contribution $r_{M_{4'}}$ of $u_{\tau,M_{4'}}$ to the kinetic energy of total ESCO flow (see Eq. (9)) for the two model configurations is shown in Fig. 4a and b, respectively. Furthermore, the spatial structure of the ESCO flow due to $u_{\tau,M_{2'}}$ and that due to $u_{\tau,M_{4'}}$ are shown in the second and third row of Fig. 4. In the flat bottom case, the ESCO flow due to the M$_{4'}$ tide is small ($r_{M_{4'}} < 0.05$) between 254 km and 256 km and dominant ($r_{M_{4'}} > 0.5$) both near the mouth ($257 < x < 260$ km) and in the upper reach ($x < 253$ km). In the sloping bottom case, it is relevant in the entire estuary. With no bottom slope, $u_{\tau,M_{2'}}$ is dominant between 253 km and 257 km, and it is seaward near the surface and
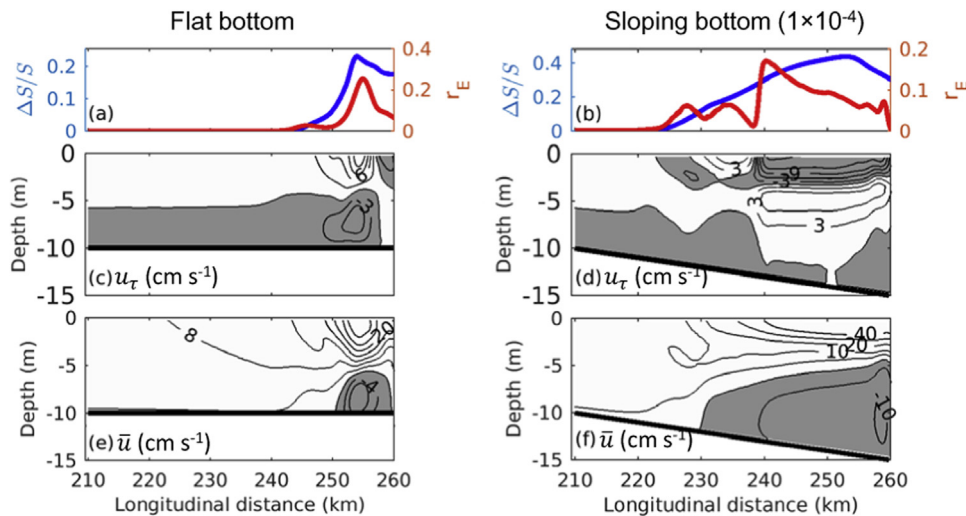

Fig. 3. (a) Longitudinal distribution of $\Delta S/S$ (blue line, with ΔS mean top to bottom salinity difference and $S = 31$ psu) and r_E of ESCO flow (red line) that contributes to depth integrated kinetic energy of total residual flow for a flat bottom case. (b) As (a), but for a bottom with slope 1×10^{-4}. (c) and (d): Contour plots of the ESCO flow (u_τ) as functions of longitudinal distance and depth for the flat bottom case and the sloping bottom case, respectively. Positive values (white areas) denote seaward and negative values (grey areas) denote landward flow. (e) and (f): as (c) and (d), but for the total residual flow ($\bar{u}$).
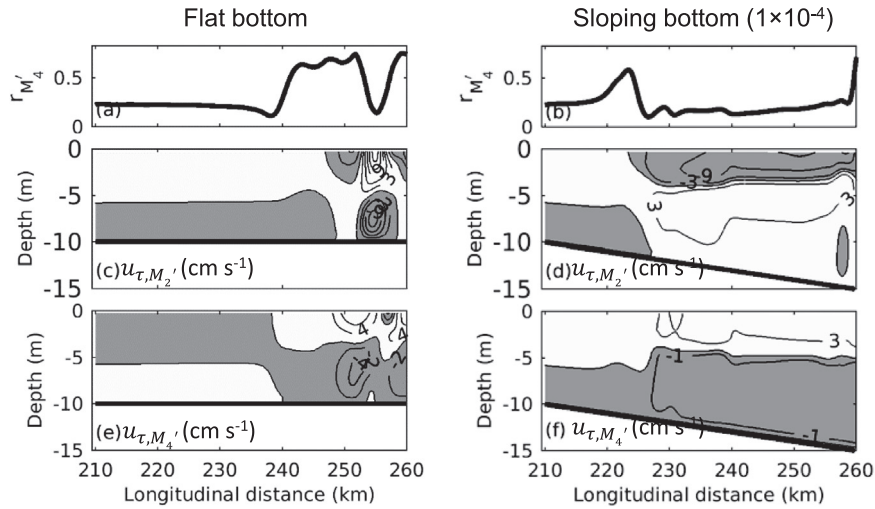
Fig. 4. (a) and (b): Longitudinal distribution of the ratio $r_{M_{4'}}$. (c) and (d): Contour plots of the ESCO flow due to the $M_{2'}$ tide ($u_{\tau,M_{2'}}$) as functions of longitudinal distance and depth for a flat bottom and a bottom with slope 1×10^{-4}, respectively. (e) and (f): As (c) and (d), but for the ESCO flow due to the $M_{4'}$ tide ($u_{\tau,M_{4'}}$). In panels (c) to (f), positive values (white areas) denote seaward and negative values (grey areas) denote landward flow.

landward near the bottom (Fig. 4c). This is similar to that of u_τ. However, further upstream and downstream, $u_{\tau,M_{2'}}$ has a reversed two-layer structure. Note that at the riverside ($x < 245$ km), $u_{\tau,M_{2'}}$ also shows a two-layer structure, but flow velocities are rather small here. In the cottom and in the sloping bottom case (Fig. 4e-f). Interestingly, for the case of the sloping bottom, near the bottom the magnitude of the landward flow of $u_{\tau,M_{4'}}$ is larger than that of the seaward flow of $u_{\tau,M_{2'}}$. The residual flow due to ESCO[a] is also computed and the energy ratio between flow due to ESCO[a] and that due to ESCO[σ] is less than 0.05 (not shown). This was also found for all other parameter settings in this study. Thus the residual flow due to ESCO[a] is not considered in the following subsections.

Next, results are presented for the experiments of series 1, 2 and 3 (see Table 1), in which the bottom slope between $x = L_e$ and $x = L_c$ was varied. Fig. 5 shows the values of the fresh water Froude number Fr_f and of parameter M (for definitions see Eq. (3)). It is found that for the bottom slope varying from 0 to 1×10^{-4}, variations of Fr_f and M in series 2 and 3 are smaller than those in series 1 (Fig. 5). When considering these data points in the regime diagram of Geyer and MacCready (2014), it follows that the largest variations in stratification due to changes in the bottom slope are obtained in the case that the
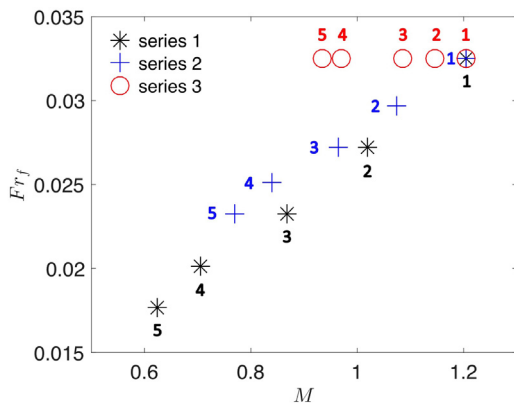

Fig. 5. Values of the fresh water Froude number Fr_f and of parameter M, which measures the ratio of the ratio of the tidal timescale to the vertical turbulent mixing timescale, of the experiments of series 1, 2 and 3. These parameters are defined in Eq. (3), and they control the stratification at the mouth. The numbers 1–5 denote the experiments in which the bottom slope between $x = L_e = 210$ km and the mouth $x = L_c = 260$ km is 0, 0.25×10^{-4}, 0.5×10^{-4}, 0.75×10^{-4}, 1×10^{-4}, respectively.

longitudinal mean depth increases (series 1). In this subsection, detailed results are presented for experiments of series 1. Additional results for experiments of series 2 and 3 are given in the Electronic Supplement.

In the case of experiment series 1, the decrease of values of Fr_f and M (Fig. 5) implies a transition of the estuary from periodically stratified to highly stratified. To identify the structure of the ESCO flow, vorticities related to the velocity profiles are calculated (see Section 2.8, Fig. 2). Fig. 6 shows vorticities in the upper layer ($\mathscr{V}_1$) and the layer below that ($\mathscr{V}_2$) as functions of longitudinal distance and bottom slope. The left, middle and right panels are results related to u_τ, $u_{\tau,M_{2'}}$ and $u_{\tau,M_{4'}}$, respectively. When the ESCO flow shows a classical two-layer structure or a reversed two-layer structure, only $\mathscr{V}_1$ exists. When the ESCO flow has a three-layer structure, both $\mathscr{V}_1$ and $\mathscr{V}_2$ exist and they have opposite signs. Note that small vorticities (absolute value below 1×10^{-3} s^{-1}) are not considered, They occur in the freshwater zone (where mean salinity is less than 1 psu) and around locations where $\mathscr{V}_1$ changes sign. The distance between black solid lines and the estuarine mouth (260 km) measures the salt intrusion length, and the latter appears to increase approximately linearly with increasing of bottom slope. Moreover, the degree of stratification ($\Delta S/S$) as a function of longitudinal distance and bottom slope is indicated by black dashed contours. Fig. 6 shows that $\mathscr{V}_1$ related to u_τ is positive (clockwise overturning) when the bottom slope is smaller than 0.1×10^{-4}. Moreover, positive $\mathscr{V}_1$ is also found near the mouth ($257 < x < 260$ km) for bottom slopes between 0 and 0.6×10^{-4}. At other locations and for other bottom slopes $\mathscr{V}_1$ is negative, and meanwhile positive $\mathscr{V}_2$ is observed. The vorticity $\mathscr{V}_1$ related to $u_{\tau,M_{2'}}$ is mainly negative for all experiments, while that related to $u_{\tau,M_{4'}}$ shows positive signs. It is also shown that larger negative values of $\mathscr{V}_1$ are obtained for larger $\Delta S/S$.

The positive vorticities in the lower layer that are related to $u_{\tau,M_{2'}}$ and $u_{\tau,M_{4'}}$ have distinct spatial structures for different bottom slopes. The vorticity $\mathscr{V}_2$ related to $u_{\tau,M_{2'}}$ is dominant near the mouth and in the middle of the estuary ($250 < x < 260$ km) when bottom slopes are smaller than 0.7×10^{-4}. However, $\mathscr{V}_2$ related to $u_{\tau,M_{4'}}$ is found near the salt intrusion limit and in the middle of the estuary when bottom slopes are larger than 0.7×10^{-4}.

Note that from vorticities $\mathscr{V}_i$ and thicknesses $H(\sigma_i - \sigma_{i+1})$ of the vorticity layers, one can compute the overturning volume transport rate per unit width, i.e., $\mathscr{T}_i = \frac{1}{2}\mathscr{V}_i H^2(\sigma_i - \sigma_{i+1})^2$. A positive (negative) value of $\mathscr{T}_i$ denotes the amount of net water per unit width that overturns clockwise (anti-clockwise) within a vorticity depth $H(\sigma_i - \sigma_{i+1})$ in layer i. Results of the thicknesses of the vorticity layers as functions of longitudinal distance and bottom slope are presented in the Electronic
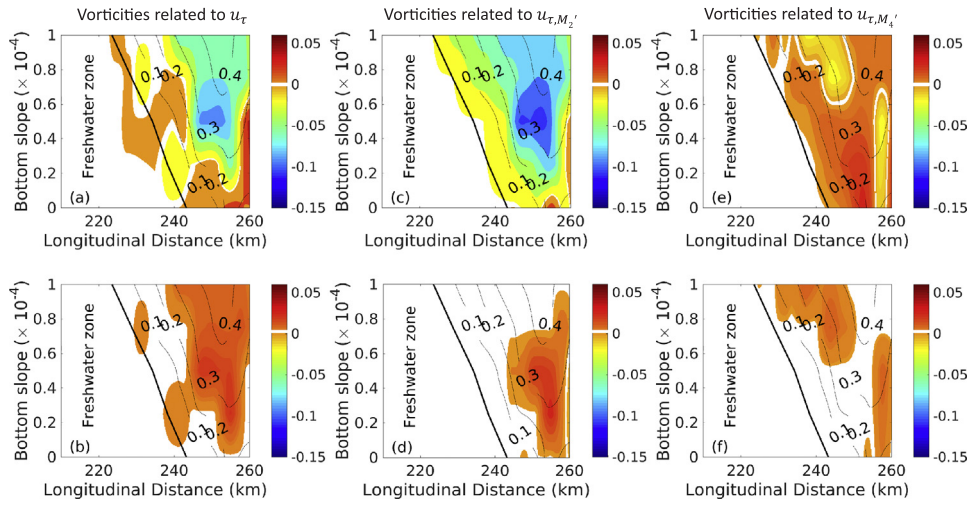
Fig. 6. Colour plots of vorticities $\mathcal{V}_1$ (upper layer, first row) and $\mathcal{V}_2$ (second layer below surface, second row) as functions of longitudinal distance and bottom slope. Unit of $\mathcal{V}_n$ is s^{-1}. Panels in the left, middle and right columns are results related to the total ESCO flow u_τ, and ESCO flows $u_{\tau,M_2'}$ and $u_{\tau,M_4'}$, respectively. Black solid lines denote the location where depth and time mean salinity is 1 psu. Areas in which vorticities $|\mathcal{V}_n| < 0.001\ s^{-1}$ are blanked. Dashed lines are contours of $\Delta S/S$.

Supplement. It turns out that typical overturning rates of ESCO flow are $\mathscr{T}_1 = 0.5\ m^3 m^{-1} s^{-1}$ for the flat bottom case and $\mathscr{T}_1 = -0.6\ m^3 m^{-1} s^{-1}$, $\mathscr{T}_2 = 0.2\ m^3 m^{-1} s^{-1}$ for the case that the bottom slope is 1×10^{-4}.

To quantify the importance of the ESCO flow $u_{\tau,M_4'}$, its relative contribution $r_{M_4'}$ to the depth-integrated kinetic energy of the total ESCO flow (see Eq. (9)) is computed for all experiments of series 1 and plotted as a function of scaled distance $\tilde{x}$ and bottom slope (Fig. 7a). Here, $\tilde{x} = (x - L_s)/(L_c - L_s)$, with L_s denoting the location of 1 psu isohaline. The salt intrusion limit is at $\tilde{x} = 0$ and the mouth is at $\tilde{x} = 1$. Hence, the freshwater zone, where the ESCO flow is small, is excluded. Results show two separate parts in the estuary where $u_{\tau,M_4'}$ is important. One is near the mouth ($0.8 < \tilde{x} < 1$) for bottom slopes smaller than 0.6×10^{-4}. The other is located inside the estuary between $0 < \tilde{x} < \tilde{x}_m$, where $\tilde{x}_m$ depends on the bottom slope and has a maximum value of 0.65. The contribution of $u_{\tau,M_4'}$ becomes negligible when the bottom slope is larger than 0.7×10^{-4}. Fig. 7b shows the relative contribution r_E of ESCO flow to the depth-integrated kinetic energy of the total residual flow as a function of scaled distance $\tilde{x}$ and bottom slope. It appears that the contribution of ESCO is relevant ($r_E > 0.05$) when $0.4 < \tilde{x} < 1$ for all bottom slopes (Fig. 7b).

Note that the river forcing together with tidal forcing determines the degree of stratification. When fixing the freshwater input at the riverside and tidal amplitude at the open boundaries, the river flow and tidal flow inside the estuary are controlled by the local depth, which changes with the bottom slope. Fig. 5 shows the relation between the

bottom slope and the degree of stratification at the mouth of the estuary. It reveals that with increasing bottom slope, the estuary becomes more stratified. For a deeper estuary, this change is more obvious.

3.2. Structure of u_τ for different tidal forcing and related changes in stratification (RA.2)

Results of experiments of series 4 are presented. In this setting, the freshwater Froude number is a constant, viz. $Fr_f = 3.2 \times 10^{-2}$. The imposed changes in the amplitude of the $M_{2'}$ tide at the seaward boundary result in values of the parameter M in the range from 0.64 to 1.55. According to the regime diagram of Geyer and MacCready (2014), these experiments simulate the estuary in conditions from highly stratified to periodically stratified.

Fig. 8 is similar to Fig. 6, but for vorticities $\mathcal{V}_1$ and $\mathcal{V}_2$ as functions of longitudinal distance and M. In panel (a), both positive and negative values of $\mathcal{V}_1$ (anticlockwise overturning) are obtained with the sign changing at $M \simeq 1.1$. In panel (b), $\mathcal{V}_2$ only shows positive values (clockwise overturning), mainly for $0.8 < M < 1.1$ and the value of $\mathcal{V}_2$ depends on the location in the estuary. The largest (both positive and negative) values of $\mathcal{V}_1$ and $\mathcal{V}_2$ are obtained at 5 km upstream from the mouth, where $\Delta S/S$ attains its maximum value. The overall distribution of $\mathcal{V}_1$ related to $u_{\tau,M_{2'}}$ (see Fig. 8c) is similar to that of $\mathcal{V}_1$ related to u_τ. However, for $1.1 < M < 1.5$, in the segments between 245 and 253 km and 257 km to the mouth, negative $\mathcal{V}_1$ is observed. Vorticity $\mathcal{V}_2$ exists
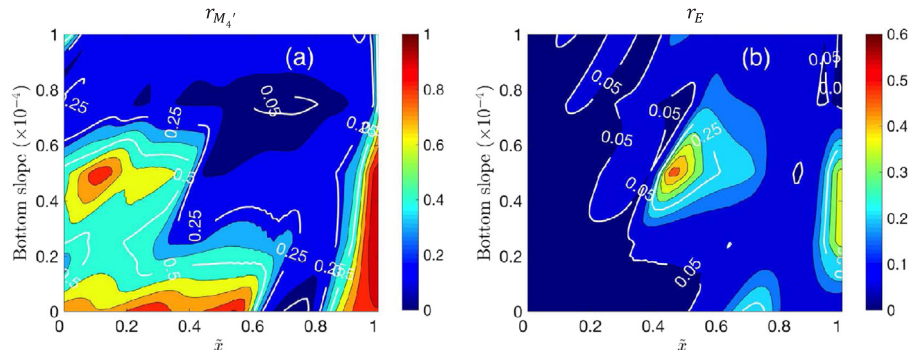

Fig. 7. a. Colour-contour plot of the relative contribution $r_{M_4'}$ as a function of scaled longitudinal distance $\tilde{x}$ and bottom slope, experiment series 1. Here, $\tilde{x} = 0$ is the location where depth and time mean salinity equals 1 psu and $\tilde{x} = 1$ is the estuary mouth. The white contour lines indicate borders in the figure where the $M_{4'}$ tide contribution to the ESCO flow is small ($r_{M_4'} < 0.05$), important ($r_{M_4'} > 0.25$) and dominant ($r_{M_4'} > 0.5$). (b): As panel (a), but for r_E. Note colour bars of panel (a) and (b) have different ranges.
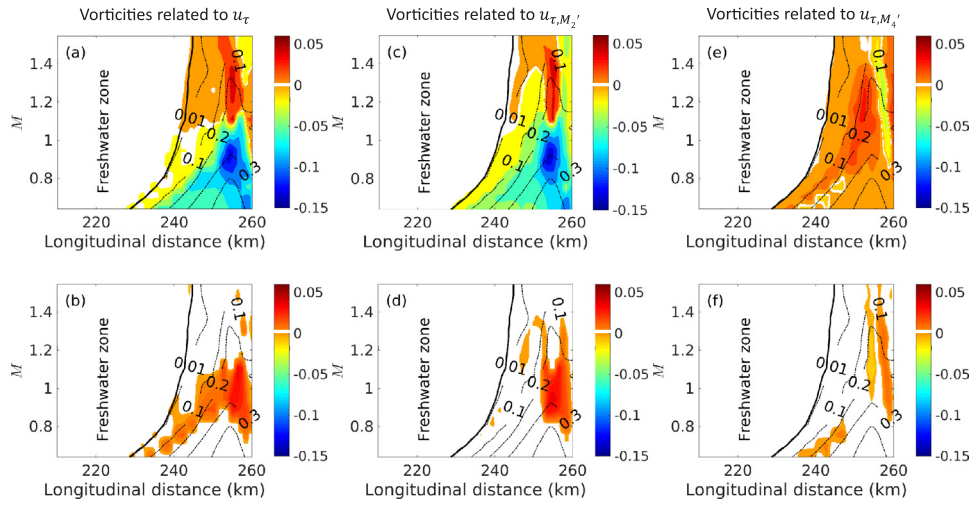
Fig. 8. As Fig. 6, but for experiment series 4: vorticities $\mathcal{V}_1$ (first row) and $\mathcal{V}_2$ (second row) are plotted as functions of longitudinal distance and parameter M that measures the tidal timescale to the vertical turbulent mixing timescale at the mouth (see Eq. (3)) for the total ESCO flow (left column), the ESCO flow due to the $M_{2'}$ tide (middle column) and due to the $M_{4'}$ tide (right column).

between $0.8 < M < 1.1$, but only between 253 km and the mouth (Fig. 8d). Contour plots of thicknesses $H(\sigma_1 - \sigma_2)$ and $H(\sigma_2 - \sigma_3)$ of the two vorticity layers as functions of $\tilde{x}$ and M are shown in the Electronic Supplement. In this series, the salt intrusion length increases non-linearly with increasing tidal forcing at the mouth.

Fig. 9 is similar to Fig. 7, and presents the energy ratio $r_{M_{4'}}$ (of the $M_{4'}$ ESCO flow and the total ESCO flow) and r_E (of the total ESCO flow and the total residual flow) for the experiments of series 4 as functions of the scaled coordinate $\tilde{x}$ and parameter M (see Eq. (3)). In the middle of the estuary, the ESCO flow is due to the $M_{2'}$ tide, where also the maximum $\Delta S/S$ is observed. For $M < 0.8$, the ESCO flow due to the $M_{4'}$ tide is always small ($r_{M_{4'}} < 0.05$). Overall, with increasing M, values of $r_{M_{4'}}$ increase, and $r_{M_{4'}} > 0.05$ is found for a wider range of $\tilde{x}$ values. When $0.9 < M < 1.4$, the ESCO flow due to the $M_{4'}$ tide $u_{\tau,M_{4'}}$ is dominant for $\tilde{x} < 0.6$ and $0.8 < \tilde{x} < 1$. The parameter $r_{M_{4'}}$ reaches its maximum value of 0.9 near the mouth and at $\tilde{x} = 0.4$. When $M > 1.4$, $u_{\tau,M_{4'}}$ becomes less intense, but it is still important for the total ESCO flow in the areas $0 < \tilde{x} < 0.25$ and $0.65 < \tilde{x} < 0.8$. Fig. 9b further reveals that values of $r_E > 0.05$ (i.e., ESCO flow significantly contributes to the total residual flow) are found mainly between $0.4 < \tilde{x} < 0.9$. The maximum value of r_E is obtained for $M = 0.9$ and $\tilde{x} = 0.7$.

For $1.1 < M < 1.4$, the modelled ESCO flow u_τ shows a classical two-layer structure in the estuary, where in the sections between 252 and 257 km, u_τ is mainly due to $u_{\tau,M_{2'}}$, and in the other sections, u_τ is due to $u_{\tau,M_{4'}}$. When $0.8 < M < 1.1$, u_τ has a three-layer structure. In the section

between 252 km and 257 km, this structure is mainly due to the $u_{\tau,M_{2'}}$. Near the mouth (257–260 km) and in the upper reach (from the location of 1 psu to 252 km), $u_{\tau,M_{4'}}$ is moderate to dominant. If $M < 0.7$, u_τ in the entire estuary is mainly due to $u_{\tau,M_{2'}}$ and it has a reversed two-layer structure. The same holds for $0.7 < M < 0.8$, but only in the middle reach.

Fig. 9 further reveals that for $M > 0.9$ and $0 < \tilde{x} < 0.4$, although the intensity of $u_{\tau,M_{4'}}$ is much larger than that of $u_{\tau,M_{2'}}$, total ESCO flow itself is negligible with respect to total residual flow ($r_E < 0.05$). For $0.9 < M < 1.1$ (weakly stratified estuaries), $u_{\tau,M_{4'}}$ is significant in the middle and lower reach ($\tilde{x} > 0.4$), where ESCO flow is an important component in the total residual flow. Moreover, although in the middle reach ($0.5 < \tilde{x} < 0.8$) $u_{\tau,M_{4'}}$ is weaker than $u_{\tau,M_{2'}}$ ($r_{M_{4'}} < 0.25$), the former is essential for obtaining a three-layer structure in the vertical distribution of the total ESCO flow.

3.3. Structure of u_τ for mixed tidal forcing (RA.3)

The effect of mixed tidal forcing on the structure of the ESCO flow is examined by analysing model results of the experiments of series 5. In each of these experiments, stratification conditions at the estuary mouth are kept fixed.

Fig. 10 is similar to Fig. 6 and it shows colour-contour plots of vorticities $\mathcal{V}_1$ (first row) and $\mathcal{V}_2$ (second row) as functions of long-itudinal distance and parameter F' (defined in Eq. (4)). Moreover,
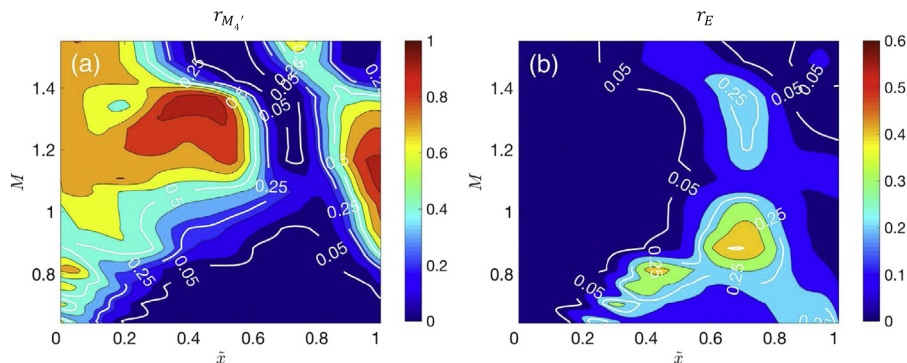

Fig. 9. As Fig. 7, but for experiments of series 4. (a): Colour-contour plot of $r_{M_{4'}}$ (relative contribution of the $M_{4'}$ ESCO flow to the depth-integrated kinetic energy of the total ESCO flow) as a function of scaled longitudinal distance $\tilde{x}$ and parameter M that measures the tidal timescale to the vertical turbulent mixing timescale at the mouth (see Eq. (3)). (b): As panel (a), but for r_E, i.e., the ratio between depth-integrated kinetic energy of the ESCO flow and that of the total residual flow. Note that colour bars of panel (a) and (b) have different ranges of values.
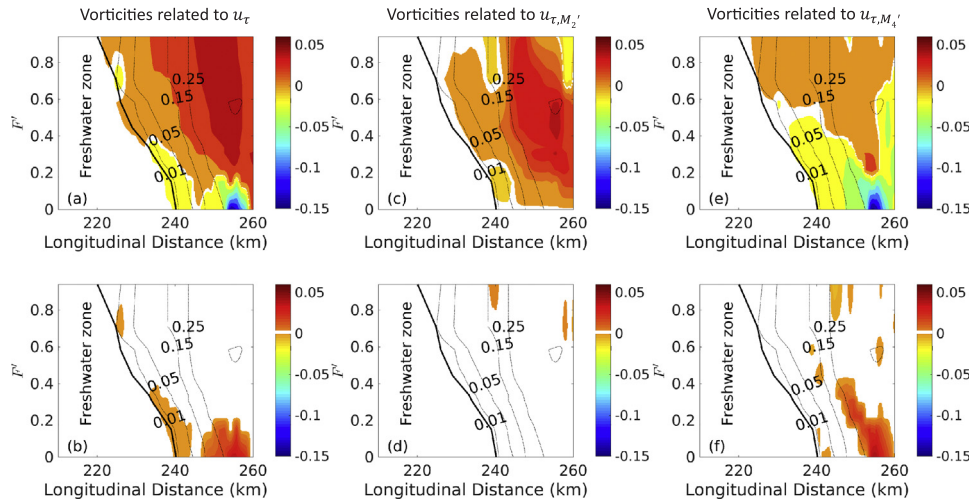
Fig. 10. As Fig. 6, but for vorticities $\mathscr{V}_1$ (first row) and $\mathscr{V}_2$ (second row) related to (left column) total ESCO flow u_τ, (middle column) the ESCO flow due to diurnal tides and (right) the ESCO flow due to semi-diurnal tides plotted as functions of longitudinal distance and parameter F' that measures the degree of mixture of externally imposed tides. Small F' (< 0.2) implies semi-diurnal tide is the dominant constituent and large F' (> 0.75) implies diurnal tides are dominant constituents.

contours of $\Delta S/S$ are shown (black dashed lines). Regarding vorticity $\mathscr{V}_1$ that is related to u_τ, negative values (anticlockwise overturning) are observed for $F' < 0.2$ and positive (clockwise overturing) for $F' > 0.2$ (Fig. 10a). Meanwhile, negative $\mathscr{V}_2$ is only found when $F' < 0.2$ (Fig. 10b). For the ESCO flow due to diurnal tides (Fig. 10c and d), positive $\mathscr{V}_1$ is observed in most of the estuary for $0 < F' < 0.6$, and between 245 and 257 km for $F' > 0.6$. The maximum positive $\mathscr{V}_1$ is obtained when $F' \simeq 0.5$. The vorticity $\mathscr{V}_2$ does not exist for this component. For the ESCO flow due to semi-diurnal tides (Fig. 10e and f), the overall distributions of $\mathscr{V}_1$ and $\mathscr{V}_2$ are similar to those of the vorticities related to u_τ, but with a much weaker clockwise overturning for $F' > 0.4$. Regarding the salt intrusion, the distance between the mouth and 1 psu location in the estuary linearly increases with increasing F'.

The vorticities due to the ESCO flow caused by ter-diurnal tides, the quarter-diurnal tide and the long-periodic tide (with frequency $2\Delta\omega$) are shown in Fig. 11. In general, $\mathscr{V}_1$ related to these ESCO components has positive values. However, each of them attain a maximum value for a different F'. For the ESCO flow due to ter-diurnal tides, the maximum $\mathscr{V}_1$ is obtained around $F' = 0.4$, while for the ESCO flow due to the quarter-diurnal tide and the long-periodic tide, the maximum $\mathscr{V}_1$ is obtained when $F' = 0$ and $F' \simeq 0.95$, respectively. In areas where the vorticity $\mathscr{V}_2$ due to the ESCO flow driven by these tide exists, its values

are negative, but rather small. Contour plots of thicknesses $H(\sigma_1 - \sigma_2)$ and $H(\sigma_2 - \sigma_3)$ of the two vorticity layers as functions of $\tilde{x}$ and F' are shown in the Electronic Supplement.

The importance of the ESCO flow due to different tidal harmonics as a function of dimensionless longitudinal distance $\tilde{x}$ and F' is shown in Fig. 12. Panels (a) to (e) show the relative contribution to the depth-integrated kinetic energy of ESCO flow driven by diurnal tides, semi-diurnal tides, ter-diurnal tides, the quarter-diurnal tide and the long-periodic tide, respectively. In panel (f), the relative contribution of the total ESCO flow to the depth-integrated kinetic energy of the total residual flow is presented. It appears that for semi-diurnal tide dominant conditions ($F' < 0.2$), the total ESCO flow is relevant in the lower reach of the estuary ($0.6 < \tilde{x} < 1$), where the main contributions to u_τ are the ESCO flow due to semi-diurnal tides (between $0.6 < \tilde{x} < 0.8$) and that due to the quarter-diurnal tide (between $0.8 < \tilde{x} < 1$). For mixed tide conditions ($0.2 < F' < 0.75$), the ESCO flow is a significant part of the total residual flow for $0.2 < \tilde{x} < 1$, where the main contribution to u_τ is the ESCO flow due to diurnal tides. Note that in the middle reach ($0.2 < \tilde{x} < 0.5$) and near the mouth ($0.8 < \tilde{x} < 1$), the ESCO flow due to ter-diurnal tides also contributes to the residual flow. For diurnal tide dominant conditions ($F' > 0.75$), the ESCO flow due to diurnal tides is significant in the area $0.5 < \tilde{x} < 0.7$; elsewhere, the main contributor to
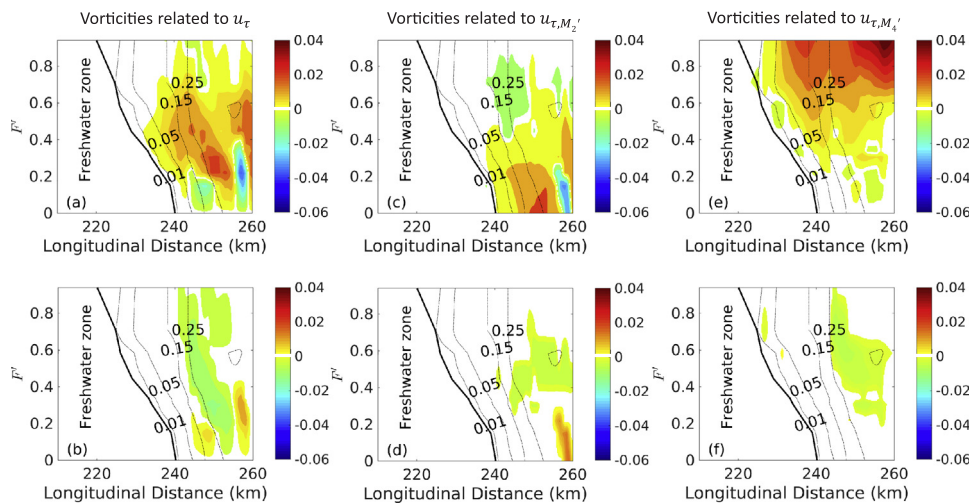

Fig. 11. As Fig. 10, but for vorticities of the ESCO flow due to ter-diurnal tides (left column), due to the quarter-diurnal tide (middle column) and due to the long-periodic tide (right column).
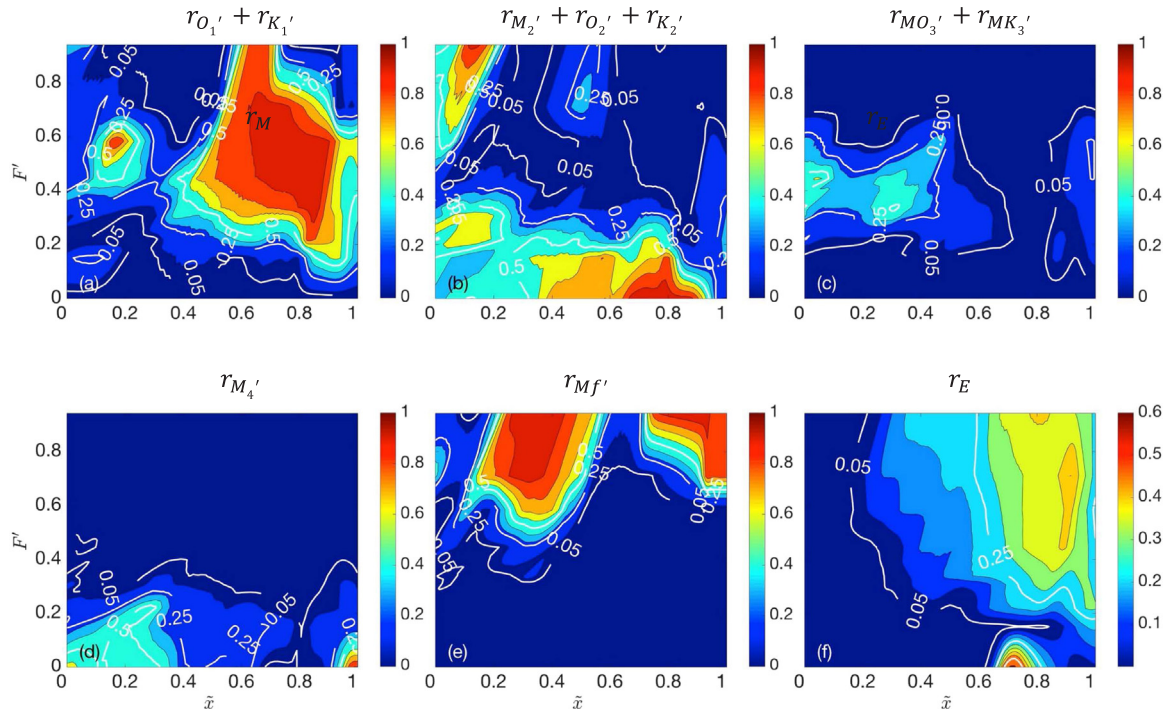
Fig. 12. (a)-(e). Colour-contour plots of ratios between depth-integrated kinetic energies of the ESCO flow driven by different tidal harmonics and the depth-integrated kinetic energy of total ESCO flow as functions of $\tilde{x}$ and F'. (f). As (a)-(e), but for the ratio between energy of the total ESCO flow and that of the total residual flow. Note panels (a)-(e) and panel (f) have different ranges of values.

u_τ is the ESCO flow due to the long-periodic tide.

4. Discussion

4.1. Analysis of vertical structures of u_τ

Sections 3.1 and 3.2 show that in a semi-diurnal tide dominant estuary the ESCO flow u_τ is mainly forced by two components that are related to $M_{2'}$ and $M_{4'}$ tides. The spatial structures of these flows strongly depend on density stratification. The vertical distribution of the ESCO flow $u_{\tau,M_{2'}}$ and $u_{\tau,M_{4'}}$ induced by the $M_{2'}$ and $M_{4'}$ tide are explained from the structure of the ESCO shear stress τ_n (Eq. (7)) and of $gH\frac{\partial\eta_{\tau,n}}{\partial x}\sigma$, where $n = M_{2'}$ or $M_{4'}$ (see Eq. (8)). The term $gH\frac{\partial\eta_{\tau,n}}{\partial x}\sigma$ is the contribution that results from integrating the barotropic pressure gradient force between level σ and the surface (the first term in the bracket of Eq. (8a)). This analysis is motivated by that of Cheng et al. (2013), who considered total ESCO flow.

First, the structure of the variables that constitute the ESCO shear stress is determined. As a specific example, this is done below for a setting of experiment series 4 (tidal forcing amplitude $A_{M_{2'}} = 1.1$ m, i.e., stratification parameter $M = 1.3$) at location $\tilde{x} = 0.6$, where $r_E \simeq 0.1$. Here, the ESCO flow is a significant component of the estuarine circulation. Fig. 13a and b show the amplitude of (blue line) the $M_{2'}$ and (red line) $M_{4'}$ component of vertical tidal shear $\left[\frac{\partial u}{\partial z}\right] = \frac{1}{H}\left[\frac{\partial u}{\partial \sigma}\right]$ and of eddy viscosity, respectively. Note that $\left[\frac{\partial u}{\partial z}\right]$ shows a local extremum at -6 m, which implies a "surface jump" shape of the $M_{2'}$ tidal current amplitude. The occurrence of such a phenomenon is physically explained by Chen and de Swart (2016). The product of the vertical tidal shear and eddy viscosity amplitude is shown in Fig. 13c, whilst panel (d) shows $\cos(\varphi_{M_{2'}} - \psi_{M_{2'}})$ and $\cos(\varphi_{M_{4'}} - \psi_{M_{4'}})$, where $\varphi_n - \psi_n$ is the phase difference between tidal shear and eddy viscosity of constituent with label n. The kinematic shear stresses τ_n, which result from the multiplication of the variables shown in panels (c) and (d), are plotted in Fig. 13e (solid lines). The dotted lines in this panel represent $gH\frac{\partial\eta_{\tau,n}}{\partial x}\sigma$. Finally, panel (f) shows the residual flow that is driven by the ESCO stress,

$u_{sh,n} = -\int_{-1}^{\sigma} H\frac{1}{A_v}\tau_n d\tilde{\sigma}$ and by $u_{ba,n} = \int_{-1}^{\sigma} H\frac{1}{A_v}gH\frac{\partial\eta_{\tau,n}}{\partial x}\tilde{\sigma}d\tilde{\sigma}$, which could be referred to as a velocity that is driven by the barotropic pressure gradient. The blue and red lines are components related to the $M_{2'}$ tide and $M_{4'}$ tide, respectively. Furthermore, in (f) the ESCO flow $u_{\tau,M_{2'}} = u_{sh,M_{2'}} + u_{ba,M_{2'}}$ and $u_{\tau,M_{4'}} = u_{sh,M_{4'}} + u_{ba,M_{4'}}$ are shown by the blue dashed line and the red dashed line, respectively.

Fig. 13 reveals that the amplitude of the $M_{2'}$ vertical tidal shear is larger than that of the $M_{4'}$ vertical tidal shear, whereas the amplitude of the $M_{2'}$ eddy viscosity is small compared to that of the $M_{4'}$ eddy viscosity. Interestingly, the product of amplitudes of vertical tidal shear and eddy viscosity of $M_{2'}$ and of $M_{4'}$ are comparable in magnitude. For the $M_{2'}$, the value of $\cos(\varphi_{M_{2'}} - \psi_{M_{2'}})$ is around -1 in the entire water column. This means that $M_{2'}$ eddy viscosity peaks for maximum flood current (large negative vertical shear), which is caused by tidal straining. For the $M_{4'}$ tidal shear and eddy viscosity, $\cos(\varphi_{M_{4'}} - \psi_{M_{4'}})$ is -1 in the upper part of the water column and around 0.5 in the lower water column. The sudden jump in $\cos(\varphi_{M_{4'}} - \psi_{M_{4'}})$ can be understood as follows. First, consider the phase $\psi_{M_{4'}}$ of $M_{4'}$ eddy viscosity $A_{v,M_{4'}}$. The primary source of $A_{v,M_{4'}}$ is tidal variation of the absolute value of the friction velocity, which peaks at $M_{2'}$ flood and ebb. Therefore $\psi_{M_{4'}} \simeq 2\varphi_{M_{2'}}$, which is almost constant over depth. Hence, the observed jump is due to the phase $\varphi_{M_{4'}}$ of $M_{4'}$ tidal shear. The latter turns out to have two important drivers, viz. $\frac{A_{v,M_{4'}}}{H}\frac{\partial\bar{u}}{\partial\sigma}$ and the $M_{4'}$ component of $\frac{A_{v,M_{2'}}}{H}\frac{\partial u_{M_{2'}}}{\partial\sigma}$. Regarding the first driver, $A_{v,M_{4'}} \sim \cos(\omega_{M_{4'}}t - 2\varphi_{M_{2'}})$, as discussed above, and the shear of the residual flow, $\frac{1}{H}\frac{\partial\bar{u}}{\partial\sigma}$, is positive. The second driver behaves like $\cos(\omega_{M_{4'}}t - \varphi_{M_{2'}})$. Since $M_{2'}$ eddy viscosity peaks at maximum flood, it follows $\psi_{M_{2'}} \simeq \varphi_{M_{2'}} + \pi$. This result implies the second driver of $M_{4'}$ tidal current shear is out of phase with the first driver. Since the drivers have different magnitudes, it means that rapid changes of $\varphi_{M_{4'}}$ over the depth may occur.

Panel (e) shows that $\tau_{M_{2'}} < 0$ in the entire water column. When ignoring the depth integrated barotropic term, the response to this shear stress is a stress $\bar{\tau} = \frac{A_v}{H}\frac{\partial\bar{u}}{\partial\sigma}$ that equals $-\tau_{M_{2'}}$. Since the velocity is zero at the bottom, it follows that $\tau_{M_{2'}}$ drives a seaward flow $u_{sh,M_{2'}}$ (see Eq. 8a) at all vertical levels, as is visible in panel (f). Since the ESCO flow must
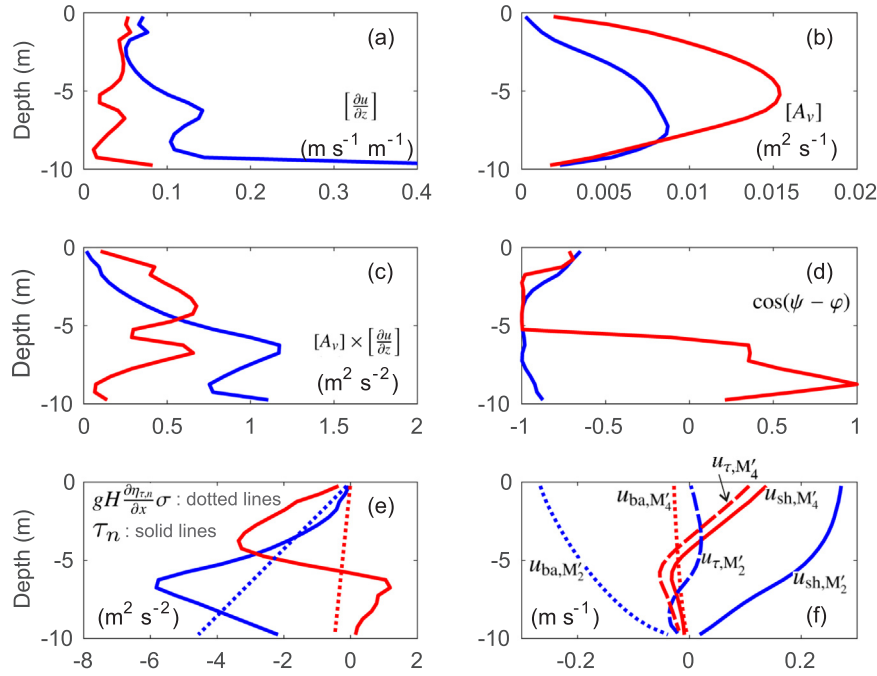
Fig. 13. Vertical distribution of variables that constitute the ESCO flow due to the $M_{2'}$ tide (blue) and $M_{4'}$ tide (red). Data for experiment series 4, with the tidal amplitude at sea boundaries of $A_{M_{2'}} = 1.1$ m at $\tilde{x} = 0.6$ (equivalent to $x = 250$ km) are plotted. Panel (a) shows amplitude of tidal shear $\left[\frac{\partial u}{\partial z}\right]$; (b) is the amplitude of eddy viscosity $[A_v]$; (c) is $[A_v] \times \left[\frac{\partial u}{\partial z}\right]$; (d) is $\cos(\psi - \varphi)$, in which φ is the phase of tidal.shear and ψ is the phase of eddy viscosity and (e) shows (solid lines) τ_n and (dotted lines) $gH\frac{\partial \eta_{\tau,n}}{\partial x}\sigma$. Panel (f) shows the residua flow $u_{sh,n}$ (solid lines) due to τ_n, $u_{ba,n}$ (dotted lines) due to the depth-integrated barotropic term and the ESCO flow $u_{\tau,n}$ (dashed lines). (For interpretation of the references to color in this figure legend, the reader is referred to the web version of this article.)

have a vanishing mean in the vertical direction, a landward directed barotropic pressure gradient force (i.e., $\frac{\partial \eta_{\tau,M_{2'}}}{\partial x} > 0$) is required, which drives a landward flow $u_{ba,M_{2'}}$. As $(gH\frac{\partial \eta_{\tau,M_{2'}}}{\partial x}\sigma - \tau_{M_{2'}}) < 0$ near the bottom (see panel (e)) and $u_{M_{2'}} = 0$ at the bottom, a landward directed $u_{M_{2'}}$ occurs near the bottom (see panel (f)). Somewhat higher in the water column, $(gH\frac{\partial \eta_{\tau,M_{2'}}}{\partial x}\sigma - \tau_{M_{2'}})$ is positive and $u_{M_{2'}}$, which results from the depth-integration of $(gH\frac{\partial \eta_{\tau,M_{2'}}}{\partial x}\sigma - \tau_{M_{2'}})$, becomes seaward towards the surface. By performing a similar analysis for $u_{\tau,M_{4'}}$, it follows that it is seaward near the surface and landward near the bottom.

The vertical profiles of the kinematic shear stresses $\tau_{M_{2'}}$ and $\tau_{M_{4'}}$ strongly depend on stratification. As is shown in Fig. 14a, when M is large (the estuary is periodically stratified), $\tau_{M_{2'}}$ and $\tau_{M_{4'}}$ both have a parabolic distribution over the vertical. The value of $(gH\frac{\partial \eta_{\tau,M_{2'}}}{\partial x}\sigma - \tau_{M_{2'}})$ and that of $(gH\frac{\partial \eta_{\tau,M_{4'}}}{\partial x}\sigma - \tau_{M_{4'}})$ are positive in the upper water layer and negative in the lower water column. In this case, both $u_{\tau,M_{2'}}$ and $u_{\tau,M_{4'}}$ have landward flow near the bottom and seaward flow near the surface, thus generates a 'classic' two-layer ESCO flow (Fig. 14d). When M is moderate (the estuary is weakly stratified), $(gH\frac{\partial \eta_{\tau,M_{2'}}}{\partial x}\sigma - \tau_{M_{2'}})$ is positive near the bottom and negative near the surface. A reversed two-layer structure is obtained in $u_{\tau,M_{2'}}$. Note that in that case $\tau_{M_{2'}}$ is positive in the upper water column, implying that $M_{2'}$ eddy viscosity peaks at ebb. The reason for this is that with increasing stratification residual flow becomes stronger and tidal flow weakens. Thus, in the upper water column, where the residual flow is seaward, the friction velocity is larger during ebb than during flood. This contributes to A_v peaking at ebb. This mechanism thus counteracts that due to tidal straining. In contrast, $(gH\frac{\partial \eta_{\tau,M_{4'}}}{\partial x}\sigma - \tau_{M_{4'}})$ is negative in the lower water column and positive in the upper water column (Fig. 14b). The residual flow $u_{\tau,M_{4'}}$ has a structure opposite to that of $u_{\tau,M_{2'}}$. Because $u_{\tau,M_{2'}}$ and $u_{\tau,M_{4'}}$ are different in the intensities at different water depth, the combination of these two components results in an ESCO flow that has a more

complicated structure (Fig. 14e). When M is small (the estuary is highly stratified), in the lower layer, $\tau_{M_{2'}}$ is significant whereas $\tau_{M_{4'}}$ is negligible (Fig. 14c). They are both small in the upper layer since turbulence is weak there. A reversed two-layer ESCO flow is obtained (Fig. 14f). Further note that the reversed two-layer structure is not found in the total estuarine circulation, which would otherwise imply a continuous increase in buoyancy. In fact, in highly stratified conditions, with decreasing M, the ESCO shear stress decreases and the ESCO flow becomes less significant compared to the density driven flow. However, ESCO weakens the overturning of the total estuarine circulation.

The above analysis explains the drop of $r_{M_{4'}}$ as shown in Fig. 3a. Moving to a location landward or seaward results in a change of the relative strength of river and tidal forcing, and thereby changes the phase differences $\varphi_{M_{2'}} - \psi_{M_{2'}}$ and $\varphi_{M_{4'}} - \psi_{M_{4'}}$. Moreover, the degree of stratification (measured by M at the mouth) also affects the vertical profile of the product of amplitudes of vertical tidal shear and eddy viscosity of a specific tidal frequency (Fig. 14). The value of $r_{M_{4'}}$ is determined when taking these two factors into account, i.e., the location in the estuary and the degree of stratification measured at the mouth.

4.2. Sensitivity of model results to the input parameters

For all model runs, horizontal eddy viscosity and diffusivity values were 50 m^{2}s^{-1}. Using A_h and K_h with values being an order of magnitude smaller slightly affects model results. For example, when A_h and K_h were set to 5 m^{2}s^{-1} in model runs, top-to-bottom salinity difference increased about 1–2 psu and the vertical eddy viscosity slightly changed (see Electronic Supplement). A further sensitivity analysis was carried out by conducting experiments with a high horizontal eddy diffusivity/viscosity coefficient (500 m^{2}s^{-1}) and with a low value of 1 m^{2}s^{-1}. In the former case, the tidal mean top-to-bottom salinity difference strongly reduced and the intensity of ESCO flow is strongly weakened, with respect to their values in the default experiment. In the latter case, the
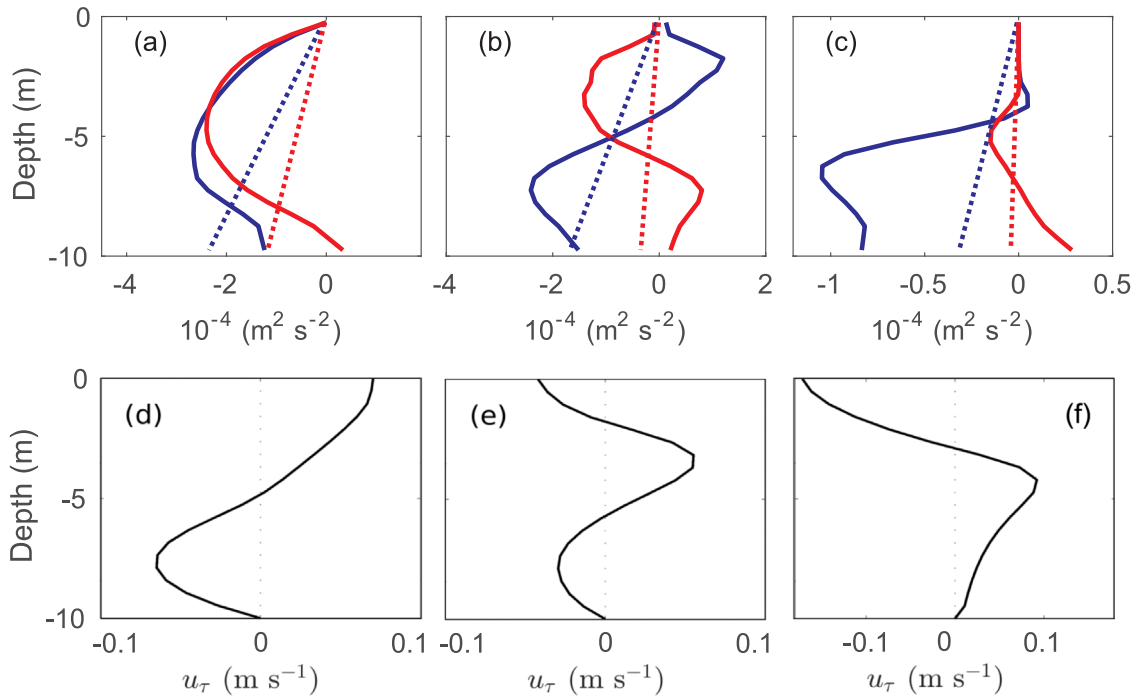
Fig. 14. Vertical distribution of shear stress components $\tau_{M_{2'}}$ (solid blue), $\tau_{M_{4'}}$ (solid red) and $gH\frac{\partial \eta_{\tau,n}}{\partial x}\sigma$ (M$_{2'}$: dashed blue, M$_{4'}$: dashed red) at (a) $\tilde{x} = 0.5$ when $M = 1.4$ (periodically stratified), at (b) $\tilde{x} = 0.6$ when $M = 1.0$ (weakly stratified) and at (c) $\tilde{x} = 0.8$ when $M = 0.7$ (highly stratified). Here $\tilde{x}$, is defined in section 3.1 and M in Eq. (3). These plots are selected such that they represent estuaries with different types of stratification but for identical values of r_E. Panels in the second row show ESCO flow in these three stratified conditions. Negative values denote landward. (For interpretation of the references to color in this figure legend, the reader is referred to the web version of this article.)

top-to-bottom salinity difference slightly increased and so did the intensity of ESCO flow. These results support the basic findings that are described in the previous sections.

To test the sensitivity of model results to the choice of frequency difference $\Delta\omega$ between $O_{1'}$ and $K_{1'}$ tide, Experiment Series 2 was re-run but for $\Delta\omega = \omega/26$. With the new value of $\Delta\omega$, one spring-neap cycle takes 6.5 days. Results of the new model runs were compared with those of the default setting (i.e., $\Delta\omega = \omega/18$, see Fig. 8). It turned out that changing $\Delta\omega$ only slightly modifies the relative importance of the ESCO flow due to individual tidal harmonics. Furthermore, the total residual salinity and flow distribution in the estuary hardly changed when compared with those of the default model runs (not shown). Hence, changing the value of $\Delta\omega$ does not affect the overall findings presented in the previous sections.

Model experiments were also conducted for the domain with smaller grid size (grid size in subdomain 2 is 150 m) and/or more vertical sigma layers (number of vertical layers is 40). Results are not sensitive to the changing of the size of cells in model domains.

4.3. Limitations

The model domain in this study is a straight channel with no lateral bottom differences. Thus the impact of lateral processes on the vertical turbulent mixing, and thereby on longitudinal ESCO flow are neglected. There are many sources that drive lateral flow and consequently change turbulent eddy viscosity and tidal velocity shear covariance. Examples of drivers are differential advection of salinity due to lateral bottom gradients (Nunes and Simpson, 1985; Lerczak and Geyer, 2004; Cheng et al., 2009), lateral advection of longitudinal tidal momentum (Lerczak and Geyer, 2004; Huijts et al., 2009, 2011), lateral gradients in turbulent mixing (Scully and Friedrichs, 2007; Basdurak et al., 2013; Cheng, 2014), channel curvature (Seim and Gregg, 1997; Chant, 2002), Coriolis (Huijts et al., 2009) and lateral flow induced by channel width convergence Burchard et al. (2014).

A second limitation of this study is that values of the radian frequencies of diurnal and semi-diurnal tidal constituents are slightly different from those in nature. Moreover, tidal constituents like the semi-diurnal solar tide $S_{2'}$ are not considered. These choices were made to keep the analysis as simple as possible. Hence, a direct comparison of modelled and observed residual flow for mixed tides conditions is not yet possible, but it is considered as an interesting topic for future work.

It appeared that the Delft3D-FLOW model is not able to capture strong vertical circulation in unstable stratified water column (weakly stratified conditions) at the subtidal time scale (Delft, 2006, chapter B.12). In our study, this occurs when $0.9 < M < 1.1$. However, it turned out that this did not affect model results at the tidal time scale (typically 12 h). This was concluded after by comparing the present model results with those of Cheng et al., (2011, 2013), who used a different numerical model (ROMS), which revealed minor differences.

Finally, note that in the present study, a weakly nonlinear system is considered (i.e., the sea surface elevation η is small compared to the water depth H). Consequently, the terms ESCO^a (in Eq. 2b), which involve triple correlation between tidally varying sea surface, eddy viscosity and tidal flow, were neglected. Moreover, the nonlinear interactions between different tidal constituents are small. Studying residual flow and ESCO flow in an estuary characterised by strong tides and highly nonlinear dynamics (Giddings et al., 2014) would be interesting to investigate in future.

5. Conclusions

This study investigated the structure of residual flow induced by covariance between tidally varying eddy viscosity and tidal velocity shear (ESCO) computed with a numerical model that was applied to an idealised estuary (straight, narrow). The total ESCO flow was decomposed into terms that are induced by individual tidal constituents. The main findings of this study are:

· The ESCO flow is significant with respect to the total residual flow

in parts of the estuary when stratification is weak to moderate.

· For estuaries forced by a single semi-diurnal tidal constituent, the ESCO flow is mainly made up by the components related to the semi-diurnal tide and to the quarter-diurnal tide. The former is dominant in the middle reach, whilst the latter is important in the upper reach and near the mouth.

· The ESCO flow due to the semi-diurnal tide has either a two-layer, three-layer or reversed two-layer structure. The occurrence of each structure depends on the degree of stratification at the mouth and the longitudinal position in the estuary. The ESCO flow due to the quarter-diurnal tide mainly shows a two-layer structure.

· For estuaries with multiple tidal forcing (mixing of a semi-diurnal tide and two diurnal tides), the ESCO flow due to diurnal tides dominates the total ESCO flow. The flow due to ter-diurnal tides also contribute to the total ESCO flow. They both show a two-layer structure in the vertical direction.

· For estuaries that are primarily forced by two diurnal tidal constituents, the ESCO flow driven by the long periodic tide, which also shows a two-layer structure, is an important component of the total ESCO flow, in particular in the upper and lower reach.

Acknowledgements

Appendix A. Supplementary data

Supplementary data associated with this article can be found in the online version at doi:10.1016/j.csr.2018.07.011.

References

Basdurak, N.B., Valle-Levinson, A., Cheng, P., 2013. Lateral structure of tidal asymmetry in vertical mixing and its impact on exchange flow in a coastal plain estuary. Cont. Shelf Res. 64, 20–32.

Burchard, H., Baumert, H., 1998. The formation of estuarine turbidity maxima due to density effects in the salt wedge. J. Phys. Oceanogr. 28, 309–321.

Burchard, H., Hetland, R.D., 2010. Quantifying the contributions of tidal straining and gravitational circulation to residual circulation in periodically stratified tidal estuaries. J. Phys. Oceanogr. 40, 1243–1262.

Burchard, H., Schulz, E., Schuttelaars, H.M., 2014. Impact of estuarine convergence on residual circulation in tidally energetic estuaries and inlets. Geophys. Res. Lett. 41, 913–919.

Burchard, H., Schuttelaars, H.M., 2012. Analysis of tidal straining as driver for estuarine circulation in well-mixed estuaries. J. Phys. Oceanogr. 42, 261–271.

Chant, R.J., 2002. Secondary circulation in a region of flow curvature: relationship with tidal forcing and river discharge. J. Geophys. Res. 107 (C9), 3131.

Chen, W., de Swart, H.E., 2016. Dynamic links between shape of the eddy viscosity profile and the vertical structure of tidal current amplitude in bays and estuaries. Ocean Dyn. 66, 299–312.

Cheng, P., 2014. Decomposition of residual circulation in estuaries. J. Atmos. Ocean. Technol. 31 (3), 698–713.

Cheng, P., de Swart, H.E., Valle-Levinson, A., 2013. Role of asymmetric tidal mixing in the subtidal dynamics of narrow estuaries. J. Geophys. Res. 118.

Cheng, P., Valle-Levinson, A., de Swart, H.E., 2010. Residual currents induced by asymmetric tidal mixing in weakly stratified narrow estuaries. J. Phys. Oceanogr. 40, 2135–2147.

Cheng, P., Valle-Levinson, A., de Swart, H.E., 2011. A numerical study of residual circulation induced by asymmetric tidal mixing in tidally dominated estuaries. J. Geophys. Res. 116, C01017.

Cheng, P., Wilson, R.E., Chant, R.J., Fugate, D.C., Flood, R.D., 2009. Modeling influence of stratification on lateral circulation in a stratified estuary. J. Phys. Oceanogr. 39 (9), 2324–2337.

de Ruijter, W.P.M., 1983. Effects of velocity shear in advective mixed-layer models. J. Phys. Oceanogr. 13 (9), 1589–1599.

Defant, A., 1958. Ebb and flow: the tides of earth, air, and water, 1st ed. University of Michigan Press, Ann Arbor, pp. 121.

Delft Hydraulics, 2006. Delft3D-FLOW user manual, Version 3.15. Delft Hydraulics, Delft, The Netherlands.

Dijkstra, Y.M., Schuttelaars, H.M., Burchard, H., 2017. Generation of exchange flows in estuaries by tidal and gravitational eddy viscosity-shear covariance (ESCO). J. Geophys. Res. Oceans 122, 4217–4237.

Geyer, W.R., MacCready, P., 2014. The estuarine circulation. Annu. Rev. Fluid Mech. 46, 175–197.

Geyer, W.R., Trowbridge, J.H., Bowen, M., 2000. The dynamics of a partially mixed estuary. J. Phys. Oceanogr. 30, 2035–2048.

Giddings, S.N., Monismith, S.G., Fong, D.A., Stacey, M.T., 2014. Using depth-normalized coordinates to examine mass transport residual circulation in estuaries with large tidal amplitude relative to the mean depth. J. Phys. Oceanogr. 44 (1), 128–148.

Huijts, K.M.H., de Swart, H.E., Schramkowski, G.P., Schuttelaars, H.M., 2011. Transverse structure of tidal and residual flow and sediment concentration in estuaries. Ocean Dyn. 61 (8), 1067–1091.

Huijts, K.M.H., Schuttelaars, H.M., de Swart, H.E., Friedrichs, C.T., 2009. Analytical study of the transverse distribution of along-channel and transverse residual flows in tidal estuaries. Cont. Shelf Res. 29, 89–100.

Ianniello, J.P., 1977. The distribution of shearing stresses in a tidal current. J. Mar. Res. 35, 755–786.

Jay, D.A., Musiak, J.D., 1994. Particle trapping in estuarine tidal flows. J. Geophys. Res. 99, 20,445–20,461.

Lacy, J.R., Stacey, M.T., Burau, J.R., Monismith, S.G., 2003. Interaction of lateral baroclinic forcing and turbulence in an estuary. J. Geophys. Res. Oceans 108 (C3).

Lerczak, J.A., Geyer, W.R., 2004. Modeling the lateral circulation in straight, stratified estuaries. J. Phys. Oceanogr. 34, 1410–1428.

Lesser, G.R., Roelvink, J.A., Van Kester, J.A.T.M., Stelling, G.S., 2004. Development and validation of a three-dimensional morphological model. Coast. Eng. 51 (8), 883–915.

Nunes, R.A., Simpson, J.H., 1985. Axial convergence in a well-mixed estuary. Estuar. Coast. Shelf Sci. 20 (5), 637–649.

Pein, J.U., Stanev, E.V., Zhang, Y.J., 2014. The tidal asymmetries and residual flows in ems estuary. Ocean Dyn. 64, 1719–1741.

Scully, M.E., Friedrichs, C.T., 2007. The importance of tidal and lateral asymmetries in stratification to residual circulation in partially mixed estuaries. J. Phys. Oceanogr. 37, 1496–1511.

Seim, H.E., Gregg, M.C., 1997. The importance of aspiration and channel curvature in producing strong vertical mixing over a sill. J. Geophys. Res. Oceans 102, 3451–3472.

Simpson, J.H., Brown, J., Matthew, J., Allen, G., 1990. Tidal straining, density currents, and stirring in the control of estuarine stratification. Estuaries 13, 125–132.

Simpson, J.H., Burchard, H., Fisher, N.R., Rippeth, T.P., 2002. The semi-diurnal cycle of dissipation in a ROFI: model-measurement comparisons. Cont. Shelf Res. 22, 1615–1628.

Simpson, J.H., Williams, E., Brasseur, L.H., Brubaker, J.M., 2005. The impact of tidal straining on the cycle of turbulence in a partially stratified estuary. Coast. Shelf Res. 25, 51–64.

Stacey, M.T., Brennan, M.L., Burau, J.R., Monismith, S.G., 2010. The tidally averaged momentum balance in a partially and periodically stratified estuary. J. Phys. Oceanogr. 40 (11), 2418–2434.

Stacey, M.T., Burau, J.R., Monismith, S.G., 2001. Creation of residual flows in a partially stratified estuary. J. Geophys. Res. 106, 17,013–17,037.

Stacey, M.T., Fram, J.P., Chow, F.K., 2008. Role of tidally periodic density stratification in the creation of estuarine subtidal circulation. J. Geophys. Res. 113, C08016.

van Aken, H.M., 1986. The onset of seasonal stratification in shelf seas due to differential advection in the presence of a salinity gradient. Cont. Shelf Res. 5, 475–485.

Verspecht, F.I., Rippeth, T.P., Souza, A.J., Burchard, H., Howarth, M.J., 2009. Residual circulation and stratification in the LiverpoolBay region of freshwater influence. Ocean Dyn. 59, 765–779.